

Nematic superconductivity in the topological semimetal CaSn_3

K. A. M. H. Siddiquee,¹ R. Munir,¹ C. Dissanayake,¹ P. Vaidya,¹ C. Nickle,¹ E. Del Barco,¹ G. Lamura,^{2,3} C. Baines,⁴ S. Cahen,⁵ C. Hérold,⁵ P. Gentile,^{6,7} T. Shiroka,^{4,8} and Y. Nakajima^{1,*}

¹Department of Physics, University of Central Florida, Orlando, Florida 32816

²CNR-SPIN, Corso Perrone 24, 16152 Genova, Italy

³Dipartimento di Fisica, Università di Genova, 16146 Genova, Italy

⁴Laboratory for Muon-Spin Spectroscopy, Paul Scherrer Institut, CH-5232 Villigen PSI, Switzerland

⁵Institut Jean Lamour, UMR 7198 CNRS-UL, 2 Allée André Guinier, B.P. 50840, 54011 Nancy Cedex, France

⁶CNR-SPIN, I-84084 Fisciano (Salerno), Italy

⁷Dipartimento di Fisica "E. R. Caianiello", Università di Salerno, I-84084 Fisciano (Salerno), Italy

⁸Laboratorium für Festkörperphysik, ETH-Hönggerberg, CH-8093 Zürich, Switzerland

(Dated: March 21, 2022)

The superconducting behavior of the topological semimetal CaSn_3 was investigated by means of magnetotransport and muon spectroscopy (μSR) measurements, both providing strong evidence of *nematic* behavior. Magnetotransport detects an anisotropic upper critical field, characterized by a twofold symmetry about C_4 axis, thus breaking the rotational symmetry of the underlying cubic lattice. Transverse-field μSR data support such picture, with the muon depolarization rate depending strongly on the magnetic field direction, here applied along the $[110]$ or $[001]$ crystal directions. In the former case, the absence of any additional muon depolarization suggests an *unconventional* vortex lattice. In the latter case, a vortex lattice encompassing a sample volume of at least 52% indicates the bulk nature of CaSn_3 superconductivity. The resulting superfluid density in the (001) planes shows a gapped low-temperature behavior, with a superconducting gap value $\Delta(0) \simeq 0.61(7)$ meV. Additional zero-field μSR results indicate that the superconducting state is time-reversal-invariant. This fact and the breaking of rotational symmetry in a fully-gapped superconductor are consistent with an unconventional pairing state in a multi-dimensional representation, thus making CaSn_3 an important example of nematic superconductor.

PACS numbers: 74.25.Op, 03.65.Vf, 74.20.Mn

I. INTRODUCTION

Topological superconductors (TSCs), hosting Majorana fermions on their boundary, have attracted considerable attention due to their potential use in quantum computing [1]. Topological superconducting states are closely linked with pairing symmetry and Fermi-surface topology. In time-reversal-invariant and inversion-symmetric systems, topological superconductivity requires odd-parity pairing with a fully-opened superconducting gap, described by $\Delta(-\mathbf{k}) = -\Delta(\mathbf{k})$, and Fermi surfaces that enclose an odd number of time-reversal-invariant momenta (TRIM) [2–4]. In spin-rotational-invariant systems, odd-parity superconductivity arises from spin-triplet pairing, mediated by ferromagnetic instabilities, as observed in UPt_3 [5]. On the other hand, in spin-orbit-coupled systems, odd-parity pairing can be stabilized even in the absence of magnetic instabilities [2].

Thanks to the presence of a strong spin-orbit coupling (SOC), the doped Bi-based topological insulator system $M_x\text{Bi}_2\text{Se}_3$ ($M = \text{Cu}, \text{Sr}, \text{Nb}$) is among the most extensively studied TSC candidate materials [6–8]. In these compounds, the topological nature of the electronic structure does not depend on doping, as confirmed by angle resolved photoemission spectroscopy (ARPES) measurements [9]. Nevertheless, a major discrepancy regarding the existence of Majorana zero modes (MZMs)

seems to occur: while point-contact spectroscopy on $\text{Cu}_x\text{Bi}_2\text{Se}_3$ shows a zero-bias conductance peak, suggestive of the presence of MZMs [10], Andreev reflection spectroscopy and STM measurements demonstrate fully-gapped superconductivity with no in-gap states, indicative of the absence of MZMs [11, 12]. Such radically different outcomes from these two surface-sensitive techniques raise serious questions about the effective realization of topological superconductivity in $M_x\text{Bi}_2\text{Se}_3$.

Recent experimental observations, however, support the unconventional pairing state associated with topological superconductivity. Several bulk probes, including nuclear magnetic resonance (NMR) [13], field-angle-resolved resistivity [14, 15], and heat-capacity measurements [16], indicate a twofold anisotropy in the basal plane, in spite of the three-fold D_{3h} symmetry of the lattice. Besides the above bulk measurements, also surface sensitive scanning tunneling microscopy (STM) measurements reveal a superconducting gap with a twofold symmetry, pinned by a mirror plane for in-plane magnetic fields [17]. The observation of a superconducting gap with twofold anisotropy indicates an odd-parity superconductivity which breaks the rotational symmetry of the underlying lattice, or nematic superconductivity. The latter is an analogue of liquid crystals, known to break the rotational symmetry while preserving translational symmetry [18]. The systematic investigation of nematic superconductivity is a pressing demand for a comprehensive understanding of topological superconductivity.

Recently, the binary stannide semimetal CaSn_3 , crystallizing in the cubic AuCu_3 -type structure with point

* Corresponding author: Yasuyuki.Nakajima@ucf.edu

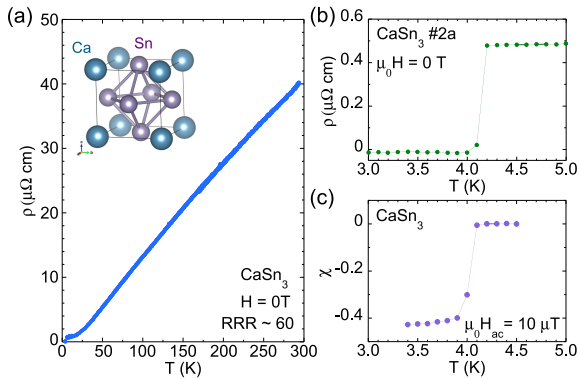


FIG. 1. (a) Inset: CaSn_3 crystallizes in the AuCu_3 -type cubic structure with a fourfold symmetry around the $\langle 100 \rangle$ -axes [23]. Main panel: Temperature dependence of resistivity showing a high residual resistivity ratio $\text{RRR} \sim 60$. (b) Low-temperature resistivity of CaSn_3 ($T < 6 \text{ K}$), showing a superconducting transition at $T_c = 4.15 \text{ K}$, consistent with the previously reported value [20]. (c) ac magnetic susceptibility of CaSn_3 [24].

group O_h [Fig. 1(a) inset], has been proposed as a prime candidate for realizing topological superconductivity [19]. This stoichiometric compound undergoes a superconducting transition at $T_c = 4.2 \text{ K}$ [20], and is predicted to be a topologically non-trivial semimetal by theoretical calculations [19]. In the absence of SOC, its electronic structure is predicted to host topological nodal lines. Upon introducing SOC, the nodal lines evolve into topological point nodes. The non-trivial Berry phase associated with the topological nature of CaSn_3 is experimentally confirmed by recent quantum oscillation measurements [21, 22]. Moreover, the Fermi surfaces determined by such measurements are shown to enclose an odd number of TRIM [22], thus fulfilling one of the two prerequisites for topological superconductivity. Clearly, it is essential to investigate whether CaSn_3 satisfies also the other prerequisite associated with the superconducting pairing states, namely, if it shows odd-parity pairing.

Here, we report on a detailed study of the superconducting state of the topological semimetal CaSn_3 . The measured upper critical fields H_{c2} show a remarkable twofold anisotropy around a C_4 axis (in a crystal structure with point group O_h). Such twofold anisotropy in the SC state cannot be attributed to an anisotropic effective mass, nor to flux-flow depinning due to the Lorentz force. Together with the peculiar temperature dependence of H_{c2} , the observation of spontaneous rotational symmetry breaking in the superconducting state for CaSn_3 clearly evidences the realization of nematic superconductivity. Muon-spin relaxation and rotation (μSR) measurements indicate a nodeless superconducting pairing state without time-reversal-symmetry breaking. Moreover, μSR measurements in magnetic fields applied along two mutually orthogonal crystal directions evidence very different electron behaviors, thus supporting nematic superconductivity in CaSn_3 . Along with a previous study, which confirms an odd number of TRIM enclosed by the Fermi surfaces of CaSn_3 , our results sug-

gest that CaSn_3 is a promising nematic superconductor candidate.

II. EXPERIMENTAL METHODS

Single crystals of CaSn_3 were grown using Sn self flux. The starting materials with a ratio of $\text{Ca}:\text{Sn} = 1:9$ were placed in an alumina crucible and sealed in a quartz tube. The quartz ampoule was heated up to 800°C , kept for 24 hours, and cooled slowly down to 300°C at a rate of 2°C/h , where the excess of molten Sn was decanted by centrifugation. Powder x-ray diffraction (XRD) results, shown in Fig. 11a, confirm the AuCu_3 -type cubic structure with a lattice constant $a = 4.7331(5) \text{ \AA}$, consistent with previous work [20]. We also confirm a stoichiometry of $\text{Ca}:\text{Sn} = 1:2.98$ with x-ray fluorescence spectroscopy, suggesting that no excess of Sn flux inclusions remain in the final samples. As reported previously [20, 21], CaSn_3 is very air-sensitive and decomposes into Sn on the surface. To avoid decomposition, we kept the crystals in a N_2 -filled glove box and minimized exposure to air while conducting magnetic and transport measurements. Cut from the same starting piece, bar-shaped samples #2a and #2b ($\sim 1.5 \times 0.50 \times 0.075 \text{ mm}^3$) were used for the angle-dependent magneto-transport measurements with a four-wire configuration in a dilution refrigerator with a Swedish rotator. Depending on the temperature range, the applied electrical currents were up to $312 \mu\text{A}$. We aligned carefully the applied current direction to the crystal axis determined from the cubic facets, so that the applied magnetic fields could rotate in a crystallographic plane within a few degrees of misalignment. We measured the ac susceptibility using a conventional mutual-inductance method with an ac driving field of $10 \mu\text{T}$ and a driving frequency of 991 Hz .

The μSR measurements were performed at the Dolly spectrometer (πE1 beamline) of the Swiss Muon Source at the Paul Scherrer Institute, Villigen, Switzerland. Experiments down to 0.27 K were carried out by using a ^3He cryostat. A mosaic of CaSn_3 single crystals was glued on a specially manufactured Ag sample holder. The full experimental details are reported in App. A. The incident muon momentum was parallel to the crystal $[110]$ direction with the external magnetic field \mathbf{H} applied parallel ($\mu_0 H_{\parallel} \neq 0$) or orthogonal ($\mu_0 H_{\perp} \neq 0$) to the $[110]$ direction. The obtained results confirm that no degradation occurred to the investigated samples (see App. B).

III. EXPERIMENTAL RESULTS

A. Resistivity Measurements

Upon lowering the temperature, the resistivity of CaSn_3 shows a metallic behavior, followed by a sharp superconducting transition at $T_c = 4.15 \text{ K}$, close to the previously reported value (Figs. 1a and 1b) [20]. The residual resistivity $\rho_0 \sim 0.5 \mu\Omega\text{cm}$, measured right above T_c ,

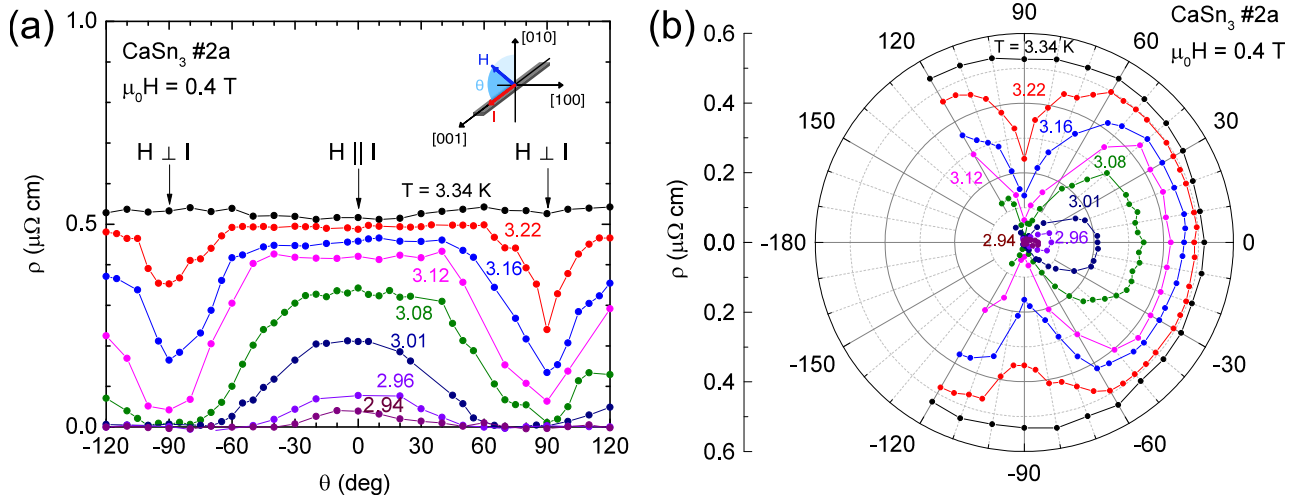


FIG. 2. (a) Resistivity as a function of θ for CaSn_3 at $\mu_0 H = 0.4 \text{ T}$ at several temperatures, where θ is the angle between the applied field H and the applied current $I \parallel [001]$. The upper critical field at $\theta = \pm 90^\circ$ ($H \perp I$) is higher than that at $\theta = 0^\circ$ ($H \parallel I$). (b) The polar plot highlights the prominent rotational-symmetry breaking in the upper critical field of CaSn_3 .

is 1000 times lower than that of the doped topological insulator $M_x\text{Bi}_2\text{Se}_3$ [14]. This result and the high residual resistivity ratio $RRR \sim 60$ suggest that the tested crystal has a low intrinsic crystalline disorder.

B. Magnetic Susceptibility

Despite a previous study [21] reporting intrinsic superconductivity below 1.2 K and surface superconductivity at 4 K (from surface decomposed Sn), here we bring unambiguous evidence of intrinsic superconductivity in CaSn_3 at $\sim 4.15 \text{ K}$ by means of ac magnetic susceptibility. In our case, we finely ground a CaSn_3 single crystal and sealed it, along with two Cu wires acting as a thermal link, in a Kapton tube with Devcon rapid epoxy (see inset of Fig. 11a in App. C). The procedure was carried out in a glove box, thus excluding any possible exposure to air. An x-ray diffraction (XRD) pattern recorded immediately before the magnetic susceptibility measurements revealed *no traces of Sn* within the threshold sensitivity of the XRD technique ($\sim 2\%$), as reported in App. C. In Fig. 1c, we show the ac magnetic susceptibility data, highlighting the onset of superconductivity at 4.15 K, consistent with the zero-resistance temperature shown in Fig. 1b. In our case, the sharpness of the transition and its onset $\sim 0.5 \text{ K}$ above that of tin $T_c = 3.72 \text{ K}$ [25] definitely rule out the presence of surface-decomposed Sn and/or of Sn inclusions, originating from the self-flux synthesis technique. A lower bound for the shielding fraction of our sample is estimated to be slightly above 40% [24]. Note that powdered samples generally show a reduced shielding due to the presence of a non-negligible fraction of grains whose size is of the same order of magnitude as the effective magnetic penetration depth. The TF- μSR results reported in Sec. III D definitely demonstrate the bulk character of superconductivity in CaSn_3 .

C. Upper Critical Fields

We performed detailed angle-dependent magnetoresistance measurements at different magnetic fields on a set of CaSn_3 single crystals. Figure 2a shows the angle-dependent resistivity $\rho(\theta)$, where θ is the angle between the electric current $I \parallel [001]$ and the applied magnetic field H . Since the AuCu_3 -type cubic structure with the point group O_h has a four-fold rotational symmetry about the (100) -axes, i.e., the C_4 axes, we expect a four-fold modulation of the physical quantities, including here the upper critical field. However, the experimental data at $\mu_0 H = 0.4 \text{ T}$ clearly show only a twofold anisotropy. It is worth noting that no distinct anisotropy of $\rho(\theta)$ is observed in the normal state at $T = 3.34 \text{ K}$, instead, it manifests itself only below $T_c(0.4 \text{ T})$. For instance, while being resistive at $\theta = 0^\circ$ ($H \parallel I \parallel [001]$) at $T = 3.08 \text{ K}$, the sample is superconducting around $\theta = \pm 90^\circ$ ($H \parallel [010] \perp I$), indicating that H_{c2} at $\theta = \pm 90^\circ$ is notably higher than that at $\theta = 0^\circ$. The spontaneous rotational symmetry breaking is even more evident in the polar plot of $\rho(\theta)$ shown in Fig. 2b. The observed angular dependence of H_{c2} can be ascribed to several effects, as described in detail below.

First of all, in the framework of the anisotropic Ginzburg-Landau (GL) model, the angular behavior of H_{c2} reflects the anisotropy of the effective mass. In this case, the angular dependence of the upper critical field is described by:

$$H_{c2}(\theta) = \frac{H_{c2}(0^\circ)}{\sqrt{\cos^2 \theta + \Gamma^{-2} \sin^2 \theta}}, \quad (1)$$

where the anisotropy ratio Γ is given by $\Gamma = H_{c2}(90^\circ)/H_{c2}(0^\circ) = \sqrt{m_{001}/m_{010}}$. Here m_{001} and m_{010} are the effective masses for the energy dispersion along the $[001]$ and $[010]$ directions, respectively. The extracted Γ from a fit to the measured angular variation of $H_{c2}(\theta)$ is 1.17, yielding an unusually large mass

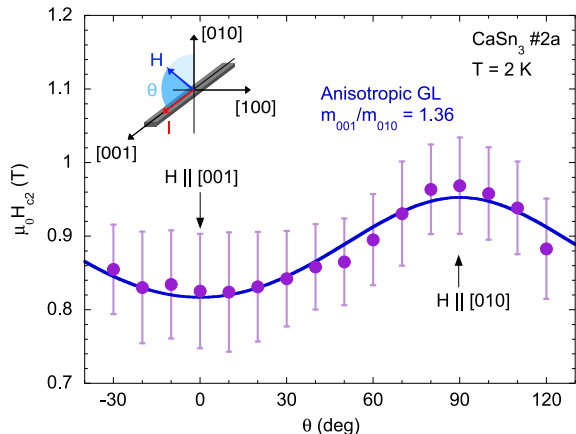


FIG. 3. Upper critical field H_{c2} obtained from the midpoints of resistive transitions as a function of θ . The error bars indicate H_{c2} determined by 10%-90% resistive transitions. The blue line is the best fit to data using the anisotropic GL model, $H_{c2}(\theta) = H_{c2}(0^\circ)/\sqrt{\cos^2 \theta + \Gamma^{-2} \sin^2 \theta}$, with extracted effective mass anisotropy $\Gamma^2 = (H_{c2}(90^\circ)/H_{c2}(0^\circ))^2 = m_{001}/m_{010}$ of 1.36 ± 0.03 and $\mu_0 H_{c2}(0^\circ) = 0.82 \pm 0.01$ T.

anisotropy of $\Gamma^2 = m_{001}/m_{010} \sim 1.36$ (Fig. 3). However, in cubic systems with a point group O_h , the effective masses along the main orthogonal axes are isotropic, i.e., $m_{001} = m_{010}$, incompatible with the values obtained for CaSn_3 , thus excluding that the twofold oscillations in H_{c2} can arise from the anisotropy of the effective mass.

Another possible explanation for the measured H_{c2} anisotropy in CaSn_3 is a lowering of symmetry due to flux-flow resistance. Since the Lorentz force depends on the relative angle between H and I , flux lines in type-II superconductors can be depinned from pinning centers. In the longitudinal configuration ($H \parallel I$), no Lorentz force is produced by the applied magnetic field. By contrast, in the transverse configurations ($H \perp I$), the applied field induces a Lorentz force, leading to a finite fluxflow resistance that reduces H_{c2} , accompanied by a broadening of the superconducting transition. The large orbital magnetoresistance caused by the Lorentz force in the normal state of CaSn_3 in the transverse configuration (Fig. 4b), $H_{c2}(90^\circ)$ ($H \perp I$), is higher than $H_{c2}(0^\circ)$ ($H \parallel I$), inconsistent with the flux-flow depinning hypothesis. Together with the absence of broadening of the resistive transition in a transverse configuration (see Figs. 4a and b), this excludes the flux-flow scenario as a cause for the observed anisotropy. We note that the observed anisotropy ($H_{c2} \perp I > H_{c2} \parallel I$) also disagrees with the anisotropy caused by Sn potentially decomposed on the surface, as this would exhibit an opposite anisotropy ($H_{c2} \parallel I > H_{c2} \perp I$) [26].

Last but not least, the unusual H_{c2} angular behavior could, in principle, originate from the lowering of the crystallographic symmetry due to a low-temperature structural phase transition. However, we did not observe any discernible anomaly — normally associated with such phase transitions — either in the temperature dependence of resistivity (Fig. 1), or in that of heat ca-

capacity [20]. In addition, the temperature-independent anisotropy of H_{c2} rules out a possible structural phase transition at or indistinguishably close to T_c . If a structural phase transition occurs at T_c , the anisotropy of H_{c2} should show a steep increase below T_c , mimicking the temperature dependence of the structural order parameter, here closely linked to the lattice distortion [27]. However, this is irreconcilable with the observed temperature dependence of H_{c2} anisotropy in CaSn_3 (lower right inset in Fig. 4c), suggesting that the crystallographic symmetry is preserved, i.e., it retains the same point group O_h , also at low temperatures. In addition, as explained later on, the twofold anisotropy of H_{c2} does not stem from a misalignment of the crystallographic axes either.

Once the GL anisotropic model and the flux-flow scenario are excluded, we can attribute the unexpected rotational symmetry breaking in the superconducting state of CaSn_3 to an unconventional pairing symmetry. Indeed, a very similar spontaneous rotational symmetry breaking in the superconducting state, or nematic superconductivity, was previously observed in $M_x\text{Bi}_2\text{Se}_3$ (a putative TSC) via field-angle-resolved resistivity [14, 15]. Here, the nematic behavior involves the odd-parity pairing symmetry described by a two-dimensional E_u representation in the trigonal D_{3d} point group of $M_x\text{Bi}_2\text{Se}_3$ [28].

In CaSn_3 , in addition to the nematic behavior, the peculiar temperature dependence of H_{c2} supports the realization of unconventional superconducting pairing. Regardless of the applied-field configuration, $H \parallel I$ or $H \perp I$, the H_{c2} of CaSn_3 extracted from the midpoints of resistive transitions (Figs. 4a and b) increases linearly with decreasing temperatures down to $T \sim 0.4T_c$, deviating from the conventional orbital depairing field described by the Werthamer-Helfand-Hohenberg (WHH) theory [29, 30]. According to the WHH theory, $H_{c2}(T)$ at $T = 0$ K is given by $H_{c2}(0) = -\alpha T_c \left. \frac{dH_{c2}}{dT} \right|_{T=T_c}$, where α is 0.69 in the dirty limit and 0.73 in the clean-limit superconductors (Fig. 4c) [29, 30]. However, the obtained values of $H_{c2}(0) = 1.4$ T for $\theta = 0^\circ$ ($H \parallel I \parallel [001]$) and 1.6 T for $\theta = 90^\circ$ ($H \parallel [010] \perp I$) correspond to $\alpha \sim 0.85$, independent of θ , substantially exceeding the orbital limit for clean superconductors $\alpha = 0.73$ (Fig. 4c inset). The overcoming of the orbital limit can be ascribed to several reasons, such as Fermi-surface topology [31, 32] or multiband effects [33]. However, an enhancement of H_{c2} due to Fermi-surface topology would reflect the anisotropy of the crystal structure. In this case, the anisotropy of H_{c2} would show a fourfold symmetry about the C_4 axes, at odds with the observed twofold oscillations. The multiband effect is also implausible, because the measured H_{c2} lacks the peculiar positive curvature of the temperature dependence of multiband superconductors, such as MgB_2 [34]. Instead, H_{c2} of CaSn_3 is in a good agreement with that of a polar p -wave pairing state [33], as shown in the inset of Fig. 4c, where we plot the normalized upper critical field $h = -H_{c2}/(T_c \left. \frac{dH_{c2}}{dT} \right|_{T=T_c})$. The good agreement between

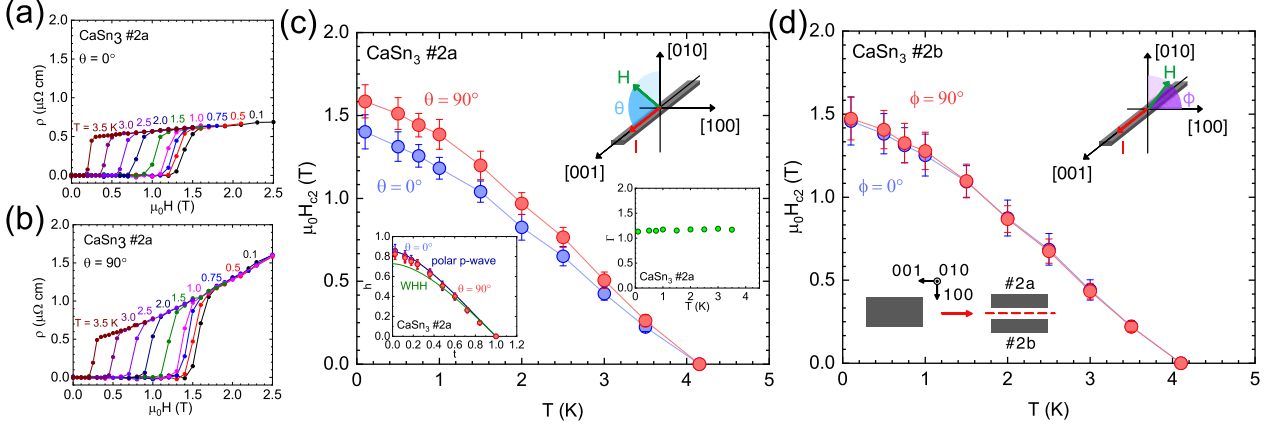


FIG. 4. Resistivity as a function of magnetic field in the configurations: (a) $H \parallel I$ ($\theta = 0^\circ$) and (b) $H \perp I$ ($\theta = 90^\circ$) for CaSn_3 (sample #2a). Here, θ is the angle between the applied field H and the current $I \parallel [001]$ (upper inset). A large magnetoresistance is observed in the $H \perp I$ configuration due to the orbital effect. (c) Temperature dependence of the upper critical field of the sample #2a for $\theta = 0^\circ$ and $\theta = 90^\circ$, obtained from the midpoint of resistive transitions with error bars indicating 10%-90% values plotted in (a) and (b). A clear breaking of the rotational symmetry is observed. The lower left inset shows the normalized upper critical field $h = -H_{c2}/(T_c \frac{dH_{c2}}{dT})|_{T=T_c}$ vs the normalized temperature $t = T/T_c$. Solid lines are theoretical curves based on the WHH theory (green) and on calculations for a polar p -wave pairing state (blue) [33]. The lower right inset depicts the anisotropy $\Gamma = H_{c2}(90^\circ)/H_{c2}(0^\circ)$ as a function of temperature. (d) Temperature dependence of the upper critical field of the sample #2b for $\phi = 0^\circ$ and $\phi = 90^\circ$, where ϕ is the angle between H and the $[100]$ axis (upper inset). The lower inset illustrates the samples #2a and #2b, cut from the same starting piece.

theory (blue line) and data suggests the realization of an unconventional pairing SC state.

Finally, it is important to note that upon rotating the magnetic field in the C_4 plane perpendicular to the applied current (ϕ rotation, from $[100]$ to $[010]$), we observe no traces of twofold anisotropy: $H_{c2}(\phi = 0^\circ) \parallel [100]$ fully overlaps with $H_{c2}(\phi = 90^\circ) \parallel [010]$, as shown in Fig. 4d. This effect cannot be ascribed to a trivial misalignment of the current direction with respect to the crystallographic axes, otherwise we would have found traces of a two-fold anisotropy, clearly not the case here. This finding indirectly confirms that the twofold anisotropy upon θ rotation is due to unconventional pairing. At the same time, it suggests that, in CaSn_3 , the nematic director is oriented along a crystallographic axis, i.e., $[001]$, presumably because of the formation of a single domain or the imbalance in multiple domains of the nematic state due to uniaxial strain fields (such as a slight lattice distortion). Evaluated from the GL relations, the superconducting coherence lengths in the $[100]$, $[010]$, and $[001]$ directions are $\xi_{100} = \xi_{010} = 153 \text{ \AA}$ and $\xi_{001} = 133 \text{ \AA}$, implying anisotropic superconducting pairing interactions due to nematicity. In $M_x\text{Bi}_2\text{Se}_3$, the nematic director does not depend on the presence or absence of an applied current [13, 15–17, 35], but it is correlated with tiny distortions of the hexagonal lattice ($\Delta a/a \sim 0.02\%$) [35]. In CaSn_3 , the upper limit of structural distortion — as estimated from peak broadening in XRD measurements — is $\Delta a/a \sim 0.06\%$, most likely associated with a pinning of the nematic director.

D. μSR measurements

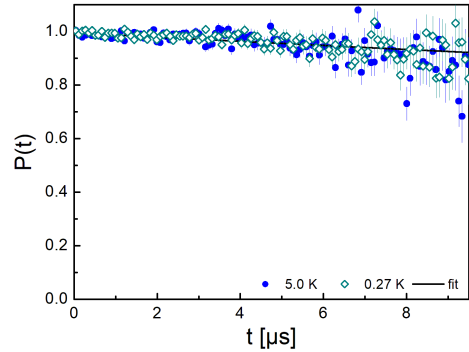


FIG. 5. Time-domain zero-field muon-spin polarizations at 0.27 K (open symbols) and at 5 K (full symbols). The line represents a simple exponential fit to the basically overlapping datasets. See text for details.

The true nature of the topological superconducting state and of its nematic properties are often controversial. To address this important issue in the CaSn_3 case, we performed systematic measurements by means of muon spectroscopy μSR , an extremely sensitive bulk probe of the local (i.e., microscopic) electronic properties. This technique uses spin-polarized positive muons implanted in the sample under test [36, 37]. Depending on the material density, μ^+ typically penetrate over a depth of several hundreds of microns and, thus, are implanted homogeneously over the whole sample volume. Consequently, muons can be considered as a bulk probe

of the local electronic properties.

We performed two kind of experiments, (i) zero-field muon spectroscopy (ZF- μ SR) and (ii) transverse-field muon spectroscopy (TF- μ SR) measurements. As to the former, we searched for the presence of possible tiny local magnetic fields, typical of, e.g., superconductors with spin-triplet pairing, as observed in Sr_2RuO_4 [38, 39] or in TSCs-like $\text{Sr}_{0.1}\text{Bi}_2\text{Se}_3$ [40]. In Fig. 5 we present the ZF time-dependent polarization below and above the superconducting transition. In both cases the experimental data are well fitted by a *purely* Gaussian decay, typically associated with the small static magnetic fields due to the randomly-oriented nuclear magnetic dipole moments on the muon implantation sites [41]. Both datasets are completely superposed, thus excluding a possible increase of the decay of polarization from spontaneous magnetic fields occurring in the superconducting state. This finding rules out the breaking of time-reversal symmetry in the superconducting state of CaSn_3 , thus excluding possible chiral superconducting states, such as $p_x \pm ip_y$ [42].

We performed TF- μ SR measurements following both standard field-cooling (FC) and nonstandard zero-field cooling (ZFC) protocols. The latter was used to evaluate the superconducting volume fraction. To this aim, after cooling down to 0.27 K in ZFC mode, we applied a magnetic field $\mu_0 H_\perp = 14$ mT along the [001] direction, orthogonal to the incident muon spin \mathbf{S}_μ (see App. A). The ZFC protocol produces rather inhomogeneous local magnetic fields at the implanted muon sites, reflecting an artificially disordered vortex lattice in the SC state. In turn, the disordered vortex lattice causes a much higher muon-spin depolarization rate (Fig. 6a) than that obtained following a conventional FC procedure (Fig. 6b) or in the normal state (Fig. 6c). The time-dependent muon-spin polarization $P(t)$ represented in Fig. 6a can be described by the following model:

$$P(t) = f_{\text{sc}} \cos(\gamma_\mu B_\mu t + \phi) \exp\left(-\frac{\sigma_n^2 + \sigma_{\text{sc}}^2}{2} t^2\right) + f_{\text{tail}} \cos(\gamma_\mu B_{\text{tail}} t + \phi) \exp(-\Lambda t). \quad (2)$$

Here, $f_{\text{sc}} = 1 - f_{\text{tail}}$ is the volume fraction of those muons probing the vortex state and, hence, it represents the superconducting fraction. f_{tail} is the fraction of muons implanted in the silver sample-holder (and in the non superconducting part of the sample), $\gamma_\mu/2\pi = 135.53$ MHz/T is the muon gyromagnetic ratio, B_μ and B_{tail} are the magnetic fields probed by muons implanted in the sample and in the silver plate, ϕ is the initial phase. σ_n and σ_{sc} are the Gaussian depolarization rates in the normal and superconducting state, respectively. σ_n is due to the static nuclear dipolar fields and it is negligibly small in this compound. Note that, in our case, σ_n cannot be distinguished from the Lorentzian relaxation rate in silver. Therefore, it was fixed to zero and an eventual nuclear dipolar contribution was accounted for by the relaxation rate of muons implanted in the silver sample holder, Λ . Such parameter was obtained by fitting the data at 5 K. The resulting value, $\Lambda = 0.005(2) \mu\text{s}^{-1}$, was kept fixed in all the subsequent fit iterations. At

the same time, the amplitude of the long-time tail of the ZFC TF- μ SR at 0.27 K (Fig. 6a) is due to those muons implanted in the silver sample-holder (and in non superconducting parts of the sample). From the initial asymmetry amplitude and its long-time value we could estimate $f_{\text{tail}} = A_{\text{tail}}/A(0)$ and, therefore, determine a *lower bound* for the superconducting volume fraction $f_{\text{sc}} = 52 \pm 1\%$, which confirms the bulk nature of superconductivity in this compound. With the same applied field ($\mu_0 H_\perp = 14$ mT in the [001] direction) we performed a TF- μ SR temperature scan, after cooling the sample in field down to base temperature. Since such procedure ensures a homogeneous flux-line lattice, in principle, it allows us to determine the superfluid density n_s , the magnetic penetration depth λ , and their temperature dependence. In Fig. 6b, we show the time-dependent muon-spin polarization $P(t)$ at 0.27 K. As expected, $P(t)$ decays more slowly than in the ZFC case (Fig. 6a). Nevertheless, such decay is still slightly faster than that measured above T_c (shown here in Fig. 6c). The depolarization rate was then extracted by fitting the time-dependent polarization data to Eq. (2) while keeping Λ , f_{Ag} , and f_{sc} fixed at all temperatures. By assuming an ideal triangular vortex lattice, since the applied field is significantly lower than the measured H_{c2} , one can link σ_{sc} to the magnetic penetration depth λ through the equation [43, 44]:

$$\frac{\sigma_{\text{sc}}^2}{\gamma_\mu^2} = 0.00371 \frac{\Phi_0}{\lambda^4}, \quad (3)$$

with Φ_0 the magnetic flux quantum. Since the magnetic field is applied along the [001] direction, Eq. (3) allows us to determine the magnetic penetration depth due to the SC screening currents flowing in the (001) planes, i.e., $\lambda_{(001)} = 910(10)$ nm at 0.27 K. From the temperature dependence of the depolarization rate σ_{sc} in the superconducting state we can extract the superfluid density $n_s(T)$ by means of the relation between n_s and σ_{sc} :

$$\frac{n_s(T)}{n_s(T_{\text{min}})} = \frac{\lambda^2(T_{\text{min}})}{\lambda^2(T)} = \frac{\sigma_{\text{sc}}(T)}{\sigma_{\text{sc}}(T_{\text{min}})}. \quad (4)$$

The normalized superfluid density $n_s(T)/n_s(T_{\text{min}})$ of CaSn_3 is shown in Fig. 7. Below $T_c \sim 4$ K, it starts to increase with decreasing temperature, to saturate at low temperatures, below $\sim T_c/3$, suggestive of a nodeless superconducting state. Data were fitted by assuming a weak-coupling Bardeen-Cooper-Schrieffer (BCS) model for the superfluid density in the clean limit [45]:

$$\frac{n_s(T)}{n_s(T_{\text{min}})} = 1 - 2 \int_{\Delta(0)}^{\infty} \left(-\frac{\partial f}{\partial E}\right) \cdot \frac{E dE}{\sqrt{E^2 - \Delta^2}}, \quad (5)$$

where $\Delta(0)$ is the energy gap at zero temperature, while its temperature dependence is assumed to be $\Delta(T)/\Delta(0) = \tanh 1.82[1.018(T_c/T - 1)]^{0.51}$ [46, 47].

The numerical fit of the normalized superfluid density to Eq. (5) is in fair agreement with the experimental data except between 1.5 and 2.5 K, where an unphysically saturated behavior still persists up to 2 K. Beyond

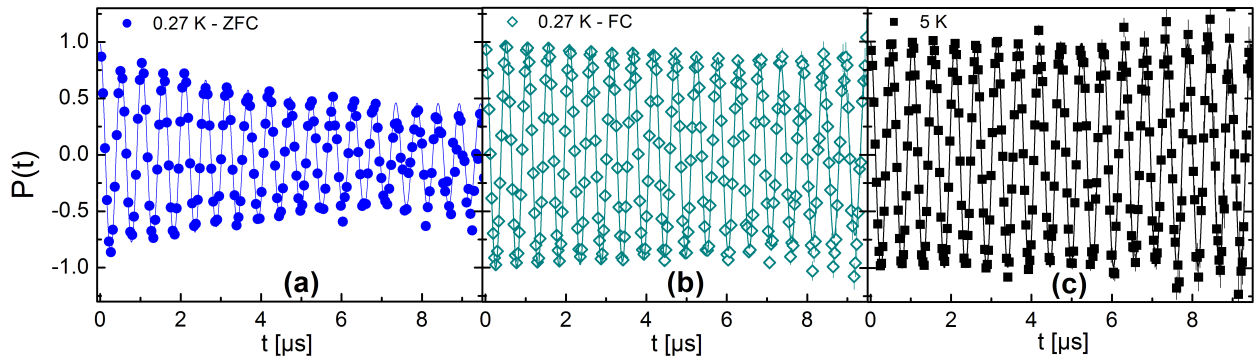


FIG. 6. Muon-spin polarization $P(t)$ in an applied field of $\mu_0 H_{\perp} = 14$ mT in the $[001]$ crystal direction at 0.27 K after ZFC (a), after FC (b), and at 5 K (c). Solid lines are fits to the model described by Eq. (2).

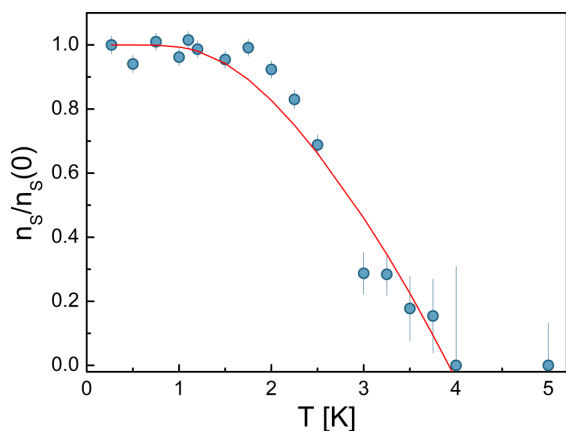


FIG. 7. Normalized superfluid density $n_s(T)/n_s(T_{min})$ in an applied magnetic field $\mu_0 H_{\perp} = 14$ mT along the $[001]$ crystal direction. The solid line is a fit to Eq. (5).

this temperature a rather sharp decrease occurs. This lack of sensitivity at intermediate temperatures could be due to the significantly low value of the measured depolarization rate. The parameters resulting from a numerical fit are $\Delta(0) \simeq 0.61(7)$ meV and $T_c \simeq 3.9(2)$ K. It is worth noting that, in CaSn_3 , both the pairing mechanism and the gap function most likely are far from those expected in standard BCS-like superconductors. Therefore, the reported values should be considered only as rough estimates.

To verify if the breakdown of rotational symmetry in CaSn_3 , observed via transport measurements through the twofold anisotropy of H_{c2} , is reflected also in its magnetic properties, we performed TF- μ SR measurements by applying the magnetic field of $\mu_0 H_{\parallel} = 30$ mT in the $[110]$ direction. Such field value is clearly in the $H_{c1} < H_{\parallel} < H_{c2}$ range, as shown by our H_{c2} measurements and by data from Ref. 20. This ensures that the sample is in its mixed superconducting state after a field cooling down to 0.27 K. In this case, we expect an ordered SC vortex state, which should induce a measurable depolarization rate in the muon-spin asymmetry. However, as shown in Fig. 8, we could not detect any

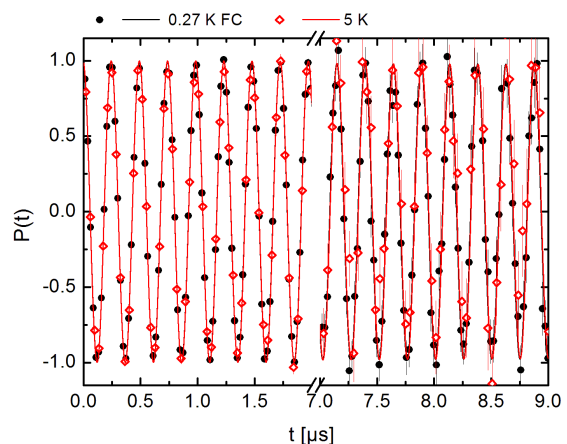


FIG. 8. Short-time and long-time TF muon-spin polarization recorded at 0.27 K (after FC) and at 5 K, in an applied magnetic field $\mu_0 H_{\parallel} = 30$ mT along the $[110]$ crystal direction. The lack of a significant muon-spin depolarization below T_c can be attributed to the presence of a non-trivial vortex phase (see text for details).

additional depolarization effects below T_c : the sample behaves as if it were in the normal state even at base temperature, clearly at odds with a $\mu_0 H_{c2}$ value of at least 1.4 T at 0.2 K (see Fig. 4). This unexpected behavior could be the fingerprint of a non-trivial vortex phase. Such unconventional picture has been predicted to occur in superconductors with a multi-component order parameter [48–50]. Therefore, the present finding represents additional evidence of nematicity in the superconducting state of CaSn_3 .

IV. DISCUSSION

Angle-resolved magnetotransport measurements in CaSn_3 show that its H_{c2} exhibits a twofold symmetry about a C_4 axis, an anisotropic behavior that breaks the rotational symmetry of the underlying crystal lattice. We ascribe this twofold anisotropy to a nematic director oriented along a crystallographic axis, as e.g., $[001]$. The

Γ	$\psi(\mathbf{k}) / d(\mathbf{k})$	Zeros in the gap	Gap structure
E_g	$k_x^2 - k_y^2$	L	
	$2k_z^2 - k_x^2 - k_y^2$	L	
T_{2g}	$k_y k_z$	L	
	$k_y k_z + i k_x k_z$	L	
E_u	$\hat{x} k_x - \hat{y} k_y$	P	
	$2\hat{z} k_z - \hat{x} k_x - \hat{y} k_y$	F	
T_{1u}	$\hat{y} k_z - \hat{z} k_y$	P	
	$\hat{x}(k_y + i k_z) - (\hat{y} + i \hat{z}) k_x$	P	
T_{2u}	$\hat{y} k_z + \hat{z} k_y$	P	
	$\hat{x}(k_y + i k_z) + (\hat{y} + i \hat{z}) k_x$	P	

TABLE I. Nematic superconducting states with D_{4h} symmetry for the point group O_h . Gap function $\psi(\mathbf{k})/d$ -vector $d(\mathbf{k})$ for each of the Γ representations with D_{4h} symmetry. We also show the corresponding type of zeros in the gap of the quasiparticle excitation spectrum (P: point nodes, L: line nodes, F: full gap), as well as a graphical representation of the gap structure [48]. The highlighted row indicates the only fully-gapped odd-parity pairing state compatible with the experimental data.

same breaking of rotational symmetry was confirmed also by μ SR measurements, which indicate a null magnetic response when the magnetic field is applied along the [110] direction, while showing a maximum response for a field applied parallel to the [001] direction. In this case, several qualitative considerations can be drawn.

First, it is particularly relevant to mention the highly unusual mixed state of $\text{Cu}_x\text{Bi}_2\text{Se}_3$, as evidenced by STM measurements [17]. Here, fields applied perpendicular to the selenium planes induce a pseudo-hexagonal vortex lattice. Interestingly, each SC vortex appears to be elongated in one direction, thus exhibiting an ellipsoidal shape. When, instead, the field was applied parallel to the Se planes, *no obvious evidence of SC vortices* could be found, despite the sample being in the mixed superconducting state and the gap successfully measured also in such configuration. This finding was justified by noting that, in a TSC, superconductivity on the surface is more robust against orbital depairing from an in-plane field, implying that the bulk vortex lines are pushed away from the surface [17]. Such scenario is inconsistent with our TF-measurements: contrary to STM, μ SR spectroscopy is a bulk technique, thus insensitive to surface states. Moreover, the absence of vortices would mean that the lower critical field in the bulk is higher than the applied field, thus resulting in a full diamagnetic effect. In such case, the implanted muons do not sense any local field, except for the small nuclear dipolar fields, almost negligible in CaSn_3 . Hence, a sizable non oscillating component in muon spin polarization and a corresponding peak at $B_\mu = 0$ in the FFT would have been detected, at odds with our experimental results (see Fig. 8 and App. B). Conversely, large and deformed vortices, far off

the scenario of conventional Abrikosov SC vortices, can give rise to unexpectedly low modulations of the local magnetic field at the muon implantation sites and, consequently, to low muon depolarization rates for applied fields *parallel* to the [001] direction, or even to a negligible modulation for applied fields *parallel* to the [110] direction.

Secondly, we find a mismatch between the carrier densities in the superconducting- n_s and in the normal state n_n of CaSn_3 . Our recent de Haas-van Alphen (dHvA) measurements provide an effective mass $m^* = 0.18m_e$ and a carrier density $n_n = 9.3 \times 10^{20} \text{ cm}^{-3}$ for the predominant hole band located at the Γ point [22]. On the other hand, utilizing $\lambda_0 = \sqrt{m^*/\mu_0 n_s e^2}$, we obtain $n_s \simeq 0.07 \times 10^{20} \text{ cm}^{-3}$, far below the reported n_n value. A similar mismatch was observed in TSCs showing a nematic character in the superconducting state, such as $\text{Cu}_x\text{Bi}_2\text{Se}_3$ and $\text{Sr}_x\text{Bi}_2\text{Se}_3$ [51, 52]. For instance, in $\text{Sr}_x\text{Bi}_2\text{Se}_3$ single crystals, $\lambda_0 \simeq 2.3 \mu\text{m}$ [52]. Hence, by assuming an effective mass of the charge carriers equal to the electron mass, one obtains $n_s \simeq 0.05 \times 10^{20} \text{ cm}^{-3}$, clearly inconsistent with $n_n \sim 1.2 \times 10^{20} \text{ cm}^{-3}$, the normal-state carrier density from low-temperature Hall-effect measurements, as reported in Ref. [52]. We believe that such inconsistency between n_s and n_n may be a common feature shared by all nematic superconductors.

Finally, we briefly comment on the possible superconducting order parameter realized in CaSn_3 . By using group-theory classifications, we can determine possible pairing symmetries, which induce a spontaneous rotational-symmetry breaking in the superconducting state of CaSn_3 . By discarding unlikely pairing states higher than the f -wave, we consider the irreducible representations of the O_h group. Then, as shown in Table I (see also Ref. 48), we classify the possible superconducting pairing states with a lower symmetry, here with a point group D_{4h} (a subgroup of O_h), which break the rotational crystallographic symmetry. Here, we assume that no admixture of pairing states is realized in CaSn_3 . Although further parity-sensitive experiments, including investigations of the NMR Knight shift, are required, the fully-gapped superconducting state without time-reversal-symmetry breaking unveiled by our μ SR measurements, together with the nematicity of CaSn_3 , suggests that a *fully-gapped* d -vector, $d(\mathbf{k}) = 2\hat{z}k_z - \hat{x}k_x - \hat{y}k_y$, in the two-dimensional representation E_u can possibly be realized in CaSn_3 (see Table I). This odd-parity state with a fully opened gap satisfies one of the key prerequisites for topological superconductivity in centrosymmetric time-reversal-invariant systems [2]. Along with the odd number of TRIM enclosed by the Fermi surfaces previously reported [22], CaSn_3 turns out to be a promising candidate material to exhibit topological superconductivity.

A. Conclusion

In conclusion, we investigated the magnetotransport and magnetic properties of the superconducting

topological semimetal CaSn_3 . We observe an unusual twofold symmetry of H_{c2} about a fourfold symmetric axis and an anomalous temperature dependence of the upper critical field, both suggestive of unconventional pairing. μSR measurements confirm the breaking of the rotational symmetry also with respect to magnetic properties, indicative of the realization of nematic superconductivity. Since ZF- μSR evidences a preserved time-reversal symmetry, while TF- μSR reveals a fully-gapped superconducting state, we can restrict a possible superconducting order parameter in CaSn_3 to the d -vector $\mathbf{d}(\mathbf{k}) = 2\hat{z}k_z - \hat{x}k_x - \hat{y}k_y$. Overall, our results suggest that the cubic CaSn_3 system fulfills one of the proposed criteria for topological superconductivity. A theoretical study addressing in full details the superconducting state emerging in CaSn_3 is planned for the next future.

ACKNOWLEDGMENTS

The authors thank K. Izawa, R. Klemm, and Y. Nagai for helpful discussions. This work was supported by startup funding from the University of Central Florida. H.S. and Y.N. were supported by NSF CAREER DMR-1944975. P.V., C.N., and E.D.B. were supported by the US NSF under Grant No. DMR-1503627. Part of this work was performed at the Swiss Muon Source μS , Paul Scherrer Institut, Villigen, Switzerland. T.S. was supported by the Swiss National Science Foundation (SNSF) (Grant No. 200021-169455).

Appendix A: μSR experimental set up

We realized a sample holder especially conceived for CaSn_3 single crystals. In Fig. 9 we show a transverse section of the sample holder, including the relative directions of the muon beam and the applied magnetic fields. The sample holder consists of high-purity (99.99%) Ag plate, where a series of 45° grooves are etched, covering an area of ca. $2 \times 2 \text{ cm}^2$. Since CaSn_3 has a cubic structure, the grooves allowed us to align its $[110]$ direction (diagonal of the faces of a cube) either parallel or orthogonal to the applied magnetic field. As shown in Fig. 9, the incident muon momentum \mathbf{p}_μ was parallel to the $[110]$ direction. In such configuration, the nematicity of CaSn_3 can be probed simply by changing the orientation of the applied magnetic field \mathbf{H} with respect to the crystal axes. Two possibilities were used: (a) \mathbf{H} parallel ($H_\parallel \neq 0$), or (b) \mathbf{H} orthogonal ($H_\perp \neq 0$) to the $[110]$ direction. We define such configurations as “parallel” and “orthogonal”, respectively. The muon spin was rotated only when the applied field was H_\parallel (WEU magnets). The CaSn_3 single crystals, depicted in blue in Fig. 9, were glued by using GE varnish [53]. The resulting mosaic covered an area of about $6 \times 6 \text{ mm}^2$. Due to the high reactivity of CaSn_3 towards oxygen and moisture, this operation was performed in a glove box under controlled atmosphere (very pure argon). The sample holder with the oriented crystals was then sealed in a glass tube by using a glass plug covered with silicone grease. Since the

sealing, too, was performed in a glove box, the samples reached the measuring site (PSI, Switzerland) without ever being exposed to air. The glass tube was opened to air for only ca. 2 minutes in order to mount the sample holder to the ^3He low-temperature insert, which was then quickly immersed in pure He gas and cooled down. Note that, despite the short exposure to air, the thin GE varnish layer covering the sample acts as a very effective protection against oxygen and moisture.

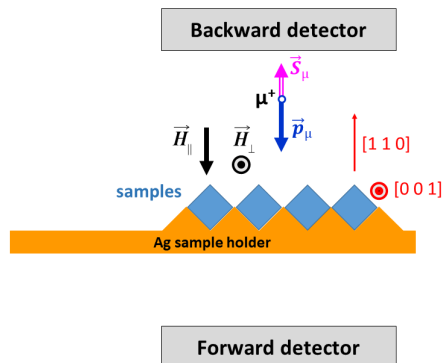


FIG. 9. Outline of the sample holder and relative positions of the positron detectors, muon beam, and applied magnetic field (WEU magnet – H_\parallel , WEV magnet – H_\perp). The red arrow and dot indicate the crystal $[110]$ and $[001]$ directions, respectively.

Appendix B: μSR test on sample degradation

CaSn_3 is particularly sensitive to oxygen and moisture, which can induce the formation of nanoscopic tin inclusions. The effect is so strong that, after some hours of exposure to air, the x-ray diffraction pattern shows only Sn peaks. Hence, to ensure that μSR data refer to a pristine sample, it is mandatory to keep its possible degradation under strict control.

Should the sample degrade during its insertion in the Heliox cryostat for the μSR measurements, two outcomes are possible. The sample may end up as a homogeneous mixture of (i) pure-, or (ii) dirty tin (i.e., tin with diluted calcium inclusions).

(i) By recalling that pure tin is a type-I superconductor, experiments in an applied field $\mu_0 H_\perp = 14 \text{ mT}$ would show peculiar features, depending if tin is in its pure diamagnetic, or in the intermediate state [54]. As to the former, the local field at the muon implantation sites should be nearly zero with a consequent absence of oscillations in the time dependent asymmetry and the presence of a zero-field peak in the corresponding FFT spectrum. As to the latter, a macroscopic separation into normal- and superconducting mesoscopic domains occurs. Thus, the time dependent polarization would consist of an oscillating term (muons stopped in the normal regions) superposed to a constant term (muons stopped in the Meissner regions). In this case, FFT spectra would show two

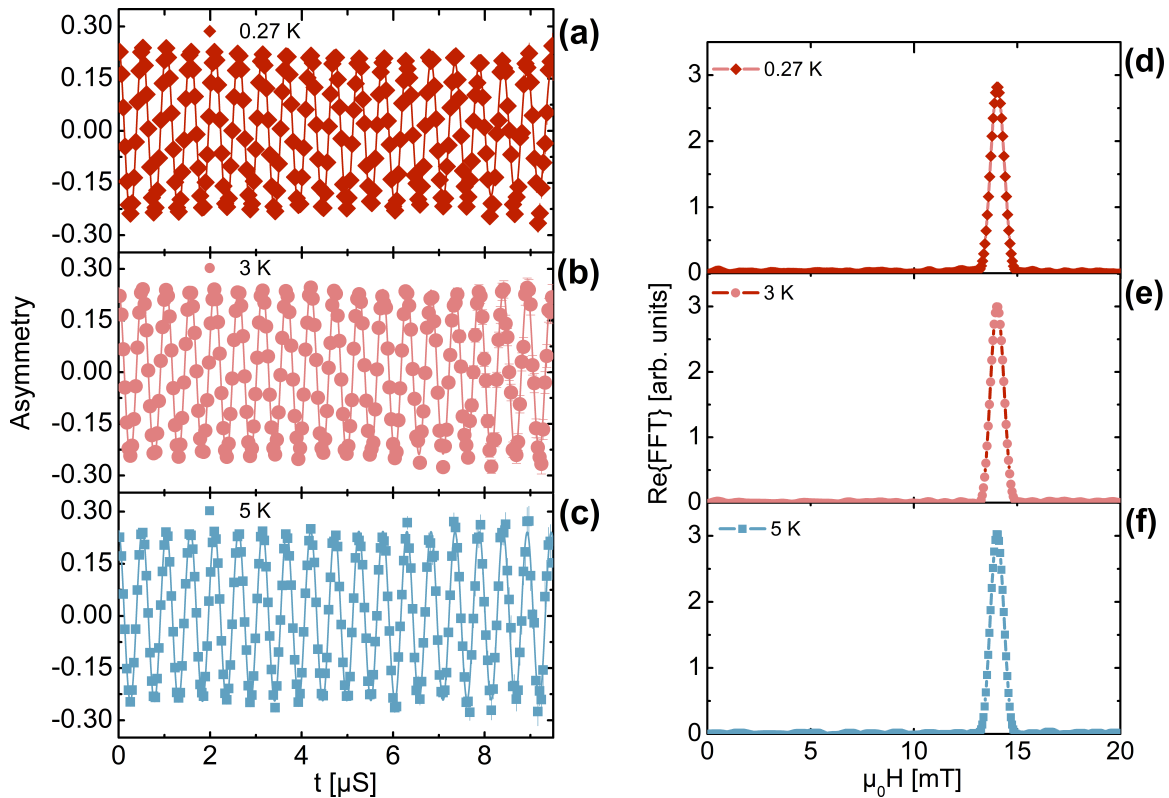


FIG. 10. (a,b,c) μ SR asymmetry measured at 0.27 K (FC), 3 K (FC), and 5 K, respectively, in an applied field $\mu_0 H_{\perp} = 14$ mT. (d,e,f) The corresponding amplitudes of the real part of FFT.

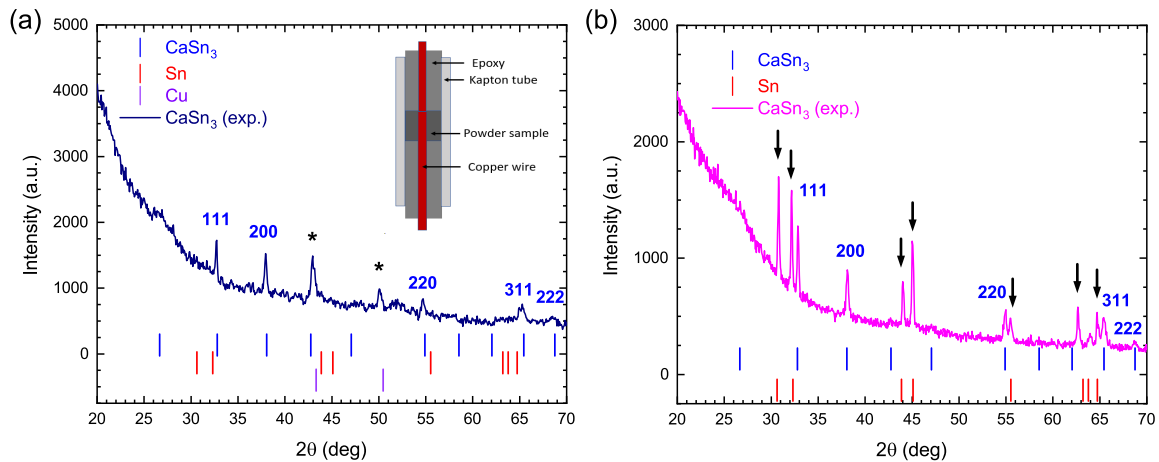


FIG. 11. X-ray diffraction pattern of CaSn_3 obtained using $\text{Cu-K}\alpha$ radiation. (a) A powder sample sealed in a Kapton tube with Devcon rapid epoxy. Asterisks indicate peaks from the Cu wires (here acting as a thermal link). No Sn peaks are observed. (b) A powder sample covered with a Kapton tape. Arrows indicate peaks from decomposed tin. Similar to previous reports [20, 21], clear degradation is observed, indicating that CaSn_3 is highly air-sensitive.

peaks, one at zero field (the superconducting fraction) and one at the thermodynamic critical field corresponding to the current temperature (the normal domains). However, as shown in Fig. 10, this is not our case.

(ii) It is well known that a type-I superconductor turns into a dirty type-II one, upon chemical substitutions and/or inclusions [55]. As deduced from x-ray measurements on degraded CaSn_3 , one can classify such system as a tin matrix with diluted Ca content. Such al-

loy should behave as dirty type-II superconductor, which preserves the isotropic character of pure tin. This is clearly not our case, since we record different types of SC behavior depending of the direction of the applied magnetic field.

Therefore, in view of the above arguments, the CaSn_3 sample studied here via μ SR can be considered pure.

Appendix C: X-ray diffraction

In Fig. 11a we show the powder x-ray diffraction pattern obtained from the sample prepared for the magnetic ac-susceptibility measurements. The sample preparation procedure is explained in detail in Sec. IIIB, while the sample holder used for the ac measurements is

shown in the inset of Fig. 11a. No discernible peaks from remaining Sn flux or from decomposed Sn are observed. For a comparison, in Fig. 11b we show the powder x-ray diffraction pattern obtained on a sample prepared following the procedure described in Ref. 21. In this case, we note the presence of Sn peaks, a clear signature of sample degradation.

-
- [1] A. P. Schnyder, S. Ryu, A. Furusaki, and A. W. W. Ludwig, *Phys. Rev. B* **78**, 195125 (2008).
- [2] L. Fu and E. Berg, *Phys. Rev. Lett.* **105**, 097001 (2010).
- [3] L. Fu, *Phys. Rev. B* **90**, 100509 (2014).
- [4] J. W. F. Venderbos, V. Kozii, and L. Fu, *Phys. Rev. B* **94**, 180504 (2016).
- [5] R. Joynt and L. Taillefer, *Rev. Mod. Phys.* **74**, 235 (2002).
- [6] Y. S. Hor, A. J. Williams, J. G. Checkelsky, P. Roushan, J. Seo, Q. Xu, H. W. Zandbergen, A. Yazdani, N. P. Ong, and R. J. Cava, *Phys. Rev. Lett.* **104**, 057001 (2010).
- [7] M. Kriener, K. Segawa, Z. Ren, S. Sasaki, and Y. Ando, *Phys. Rev. Lett.* **106**, 127004 (2011).
- [8] Shruti, V. K. Maurya, P. Neha, P. Srivastava, and S. Patnaik, *Phys. Rev. B* **92**, 020506 (2015).
- [9] L. A. Wray, S.-Y. Xu, Y. Xia, Y. S. Hor, D. Qian, A. V. Fedorov, H. Lin, A. Bansil, R. J. Cava, and M. Z. Hasan, *Nat. Phys.* **6**, 855 (2010).
- [10] S. Sasaki, M. Kriener, K. Segawa, K. Yada, Y. Tanaka, M. Sato, and Y. Ando, *Phys. Rev. Lett.* **107**, 217001 (2011).
- [11] H. Peng, D. De, B. Lv, F. Wei, and C.-W. Chu, *Phys. Rev. B* **88**, 024515 (2013).
- [12] N. Levy, T. Zhang, J. Ha, F. Sharifi, A. A. Talin, Y. Kuk, and J. A. Stroscio, *Phys. Rev. Lett.* **110**, 117001 (2013).
- [13] K. Matano, M. Kriener, K. Segawa, Y. Ando, and G.-q. Zheng, *Nat. Phys.* **12**, 852 (2016).
- [14] Y. Pan, A. M. Nikitin, G. K. Arazizi, Y. K. Huang, Y. Matsushita, T. Naka, and A. de Visser, *Sci. Rep.* **6**, 28632 (2016).
- [15] M. P. Smylie, K. Willa, H. Claus, A. E. Koshelev, K. W. Song, W. K. Kwok, Z. Islam, G. D. Gu, J. A. Schneeloch, R. D. Zhong, and U. Welp, *Sci. Rep.* **8**, 7666 (2018).
- [16] S. Yonezawa, K. Tajiri, S. Nakata, Y. Nagai, Z. Wang, K. Segawa, Y. Ando, and Y. Maeno, *Nat. Phys.* **13**, 123 (2017).
- [17] R. Tao, Y.-J. Yan, X. Liu, Z.-W. Wang, Y. Ando, Q.-H. Wang, T. Zhang, and D.-L. Feng, *Phys. Rev. X* **8**, 041024 (2018).
- [18] E. Fradkin, S. A. Kivelson, M. J. Lawler, J. P. Eisenstein, and A. P. Mackenzie, *Annu. Rev. Condens. Matter Phys.* **1**, 153 (2010).
- [19] S. Gupta, R. Juneja, R. Shinde, and A. K. Singh, *J. Appl. Phys.* **121**, 214901 (2017).
- [20] X. Luo, D. F. Shao, Q. L. Pei, J. Y. Song, L. Hu, Y. Y. Han, X. B. Zhu, W. H. Song, W. J. Lu, and Y. P. Sun, *J. Mater. Chem. C* **3**, 11432 (2015).
- [21] Y. L. Zhu, J. Hu, F. N. Womack, D. Graf, Y. Wang, P. W. Adams, and Z. Q. Mao, *J. Phys. Condens. Matter* **31**, 245703 (2019).
- [22] K. A. M. H. Siddiquee, R. Munir, C. Dissanayake, X. Hu, S. Yadav, Y. Takano, E. S. Choi, D. Le, T. S. Rahman, and Y. Nakajima, *J. Phys. Condens. Matter* **33**, 17LT01 (2021).
- [23] K. Momma and F. Izumi, *J. Appl. Crystallogr.* **44**, 1272 (2011).
- [24] The magnetic susceptibility was calculated by assuming a demagnetizing factor $N = 1/3$, i.e., by considering the powder sample to consists of spherical grains.
- [25] C. H. Pool, H. A. Farach, R. J. Creswick, and R. Prozorov, *Superconductivity* (Academic Press, London, 2007) second Edition.
- [26] F. E. Harper and M. Tinkham, *Phys. Rev.* **172**, 441 (1968).
- [27] J. D. Axe and G. Shirane, *Phys. Rev. B* **8**, 1965 (1973).
- [28] J. W. F. Venderbos, V. Kozii, and L. Fu, *Phys. Rev. B* **94**, 094522 (2016).
- [29] N. Werthamer, E. Helfand, and P. Hohenberg, *Phys. Rev.* **147**, 295 (1966).
- [30] E. Helfand and N. R. Werthamer, *Phys. Rev.* **147**, 288 (1966).
- [31] T. Kita and M. Arai, *Phys. Rev. B* **70**, 224522 (2004).
- [32] T. Shibauchi, L. Krusin-Elbaum, Y. Kasahara, Y. Shimono, Y. Matsuda, R. D. McDonald, C. H. Mielke, S. Yonezawa, Z. Hiroi, M. Arai, T. Kita, G. Blatter, and M. Sigrist, *Phys. Rev. B* **74**, 220506 (2006).
- [33] K. Scharnberg and R. A. Klemm, *Phys. Rev. B* **22**, 5233 (1980).
- [34] A. Gurevich, S. Patnaik, V. Braccini, K. Kim, C. Mielke, X. Song, L. Cooley, S. Bu, D. Kim, J. Choi, L. Belenky, J. Giенcke, M. Lee, W. Tian, X. Pan, A. Siri, E. Hellstrom, C. Eom, and D. Larbalestier, *Supercond. Sci. Tech.* **17**, 278 (2004).
- [35] A. Kuntsevich, M. A. Bryzgalov, V. A. Prudkoglyad, V. P. Martovitskii, Y. G. Selivanov, and E. G. Chizhevskii, *New J. Phys.* **20**, 103022 (2018).
- [36] S. J. Blundell, *Contemp. Phys.* **40**, 175 (1999).
- [37] A. Amato, *Rev. Mod. Phys.* **69**, 1119 (1997).
- [38] G. M. Luke, Y. Fudamoto, K. M. Kojima, M. I. Larkin, J. Merrin, B. Nachumi, Y. J. Uemura, Y. Maeno, Z. Q. Mao, Y. Mori, H. Nakamura, and M. Sigrist, *Nature* **394**, 558 (1998).
- [39] T. Shiroka, R. Fittipaldi, M. Cuoco, R. De Renzi, Y. Maeno, R. J. Lycett, S. Ramos, E. M. Forgan, C. Baines, A. Rost, V. Granata, and A. Vecchione, *Phys. Rev. B* **85**, 134527 (2012).
- [40] P. Neha, P. K. Biswas, T. Das, and S. Patnaik, *Phys. Rev. Mater.* **3**, 074201 (2019).
- [41] A. Yaouanc and P. Dalmas de Réotier, *Muon Spin Rotation, Relaxation, and Resonance: Applications to Condensed Matter* (Oxford University Press, Oxford, 2011).
- [42] C. Kallin and J. Berlinsky, *Rep. Prog. Phys.* **79**, 054502 (2016).
- [43] W. Barford and J. M. F. Gunn, *Physica C* **156**, 515 (1988).
- [44] E. H. Brandt, *Phys. Rev. B* **68**, 054506 (2003).
- [45] M. Tinkham, *Introduction to Superconductivity* (MacGraw Hill, Inc., 1996).
- [46] A. Carrington and F. Manzano, *Physica C* **385**, 205 (2003).
- [47] R. Khasanov, A. Shengelaya, A. Maisuradze, D. Di Castro, I. M. Savić, S. Weyeneth, M. S. Park, D. J. Jang, S.-I. Lee, and H. Keller, *Phys. Rev. B* **77**, 184512 (2008).

- [48] M. Sigrist and K. Ueda, *Rev. Mod. Phys.* **63**, 239 (1991).
- [49] A. A. Zyuzin, J. Garaud, and E. Babaev, *Phys. Rev. Lett.* **119**, 167001 (2017).
- [50] P. T. How and S.-K. Yip, *Phys. Rev. Research* **2**, 043192 (2020).
- [51] J. A. Krieger, A. Kanigel, A. Ribak, E. Pomjakushina, K. B. Chashka, K. Conder, E. Morenzoni, T. Prokscha, A. Suter, and Z. Salman, *JPS Conf. Proc.* **21**, 011028 (2018).
- [52] H. Leng, D. Cherian, Y. K. Huang, J.-C. Orain, A. Amato, and A. de Visser, *Phys. Rev. B* **97**, 054503 (2018).
- [53] Before using the GE varnish, we checked that it does not degrade the as-grown CaSn_3 single crystals.
- [54] R. Karl, F. Burri, A. Amato, M. Donegà, S. Gvasaliya, H. Luetkens, E. Morenzoni, and R. Khasanov, *Phys. Rev. B* **99**, 184515 (2019).
- [55] J. D. Livingston, *Phys. Rev.* **129**, 1943 (1963).